Remote Sensing of Environment 129 (2013) 132–143

Contents lists available at SciVerse ScienceDirect

Remote Sensing of Environment

journal homepage: www.elsevier.com/locate/rse

A small-scale oceanic eddy off the coast of West Africa studied by multi-sensor satellite and surface drifter data

Werner Alpers [a], Peter Brandt [b,*], Alban Lazar [c], Dominique Dagorne [d], Bamol Sow [e,f], Saliou Faye [f,g], Morten W. Hansen [h], Angelo Rubino [i], Pierre-Marie Poulain [j], Patrice Brehmer [g,k]

[a] Institute of Oceanography, Center for Earth System Research and Sustainability, University of Hamburg, Bundesstrasse 53, D-20146 Hamburg, Germany
[b] GEOMAR Helmholtz-Zentrum für Ozeanforschung Kiel, Düsternbrooker Weg 20, D-24105 Kiel, Germany
[c] LOCEAN-IPSL (UPMC,IRD,CNRS,MNHN), Université Pierre et Marie Curie, 4 pl. Jussieu, 75252 Paris cedex 05, France
[d] Institut de Recherche pour le Développement, US Imago, BP70, F-29280 Plouzané, France
[e] Laboratoire d'Océanographie, des Sciences de l'Environnement et du Climat, Université de Ziguinchor, BP 523, Ziguincho, Sénégal
[f] Laboratoire de Physique de l'Atmosphère et de l'Océan, Siméon Fongang, ESP/UCAD, BP 5085, Dakar-Fann, Sénégal
[g] Institut Sénégalais de Recherche Agronomique, Centre de Recherche Océanographique Dakar-Thiaroye (CRODT), BP 2241, Dakar, Sénégal
[h] Nansen Environmental and Remote Sensing Center, Thormoehlensgate 47, N-5006, Bergen, Norway
[i] Università Ca' Foscari di Venezia, Dipartimento di Scienze Ambientali, Calle Larga Santa Marta, Dorsoduro 2137, I-30123 Venezia, Italy
[j] Istituto Nazionale di Oceanografia e di Geofisica Sperimentale (OGS), Borgo Grotta Gigante, 42/c, 34010 Sgonico (Trieste), Italy
[k] Institut de Recherche pour le Développement, UMR LEMAR (CNRS, UBO, IRD, IFREMER), BP 70, F-29280 Plouzané, France

ARTICLE INFO

Article history:
Received 23 May 2012
Received in revised form 9 October 2012
Accepted 28 October 2012
Available online 29 November 2012

Keywords:
Small-scale eddy
Trade winds
Coastal upwelling
SST
Chlorophyll-a
MODIS
SAR
Surface drifter
West Africa
Cap-Vert

ABSTRACT

A small-scale oceanic eddy, which was generated in autumn 2011 at the headland of Cap-Vert off the coast of Senegal, West Africa, and then propagated westward into the open North Atlantic Ocean, is studied by multi-sensor satellite and surface drifter data. The eddy was generated after a sudden increase of the trade winds causing an enhanced southward flow and upwelling at the coast of Senegal. After this wind burst event, an extremely nonlinear cyclonic eddy with a radius of about 10 to 20 km evolved downstream of Cap-Vert with Rossby number larger than one. Our analysis suggests that the eddy was generated by flow separation at the headland of Cap-Vert. The eddy was tracked on its way into the open North Atlantic Ocean from satellites over 31 days via its sea surface temperature and chlorophyll-a (CHL) signature and by a satellite-tracked surface drifter. The satellite images show that this small-scale eddy transported nutrients from the upwelling region westward into the oligotrophic North Atlantic thus giving rise to enhanced CHL concentration there. Maximum CHL concentration was encountered few days after vortex generation, which is consistent with a delayed plankton growth following nutrient supply into the euphotic zone within the eddy. Furthermore, the eddy was imaged by the synthetic aperture radar (SAR) onboard the Envisat satellite. It is shown that the radar signatures of cold eddies result from damping of short surface waves by biogenic surface films which arise from surface-active material secreted by the biota in the cold eddy as well as by the change of the stability of the air–sea interface.

1. Introduction

Oceanic eddies of horizontal scales ranging from several hundred meters to several hundred kilometers have often been observed from satellites. An excellent means to study eddies with horizontal scales above 100 km are radar altimeters which presently fly on several satellites. Radar altimeters measure eddies via sea level anomalies (SLA) and use the geostrophic approximation to retrieve current velocities (see, e.g., Chelton et al., 2011a; Scott et al., 2010). Eddies are encountered all over the World's ocean (see, e.g., Cresswell & Legeckis, 1986; Stevenson, 1998; Siegel et al., 2001). Chaigneau et al. (2008) have investigated eddy activity in the Canary upwelling area (10–45°N; 40–5°W) by using 15 years of satellite altimetry data. Restricting their analysis to long-lived eddies having SLA larger than 2 cm and lifetimes larger than 35 days, they found that, on the average, around 60–100 eddies with diameters of 140–320 km are present on weekly maps and that 4–7 eddies are generated each week in this area. Preferred regions of eddy generation are those of strong currents, like the Gulf Stream, and upwelling regions, like the Canary upwelling area.

However, eddies with horizontal scales below 50 km (or more realistically: below 100 km) cannot be resolved by conventional altimeters (Fu & Ferrari, 2008), but they can be observed from space by high-resolution optical/infrared sensors and by synthetic aperture radars (SARs). In this paper we call eddies with diameters smaller than 50 km small-scale eddies, although, in the literature, their names are often chosen according to their dynamical or morphological properties. Sometimes such features are called sub-mesoscale eddies (Bassin

* Corresponding author. Tel.: +49 431 600 4105.
E-mail address: pbrandt@geomar.de (P. Brandt).

0034-4257/$ – see front matter © 2012 Elsevier Inc. All rights reserved.
http://dx.doi.org/10.1016/j.rse.2012.10.032

et al., 2005; Fu & Ferrari, 2008; McWilliams, 1985) or spiral eddies (Eldevik & Dysthe, 2002; Karimova, 2012). We have refrained here from using the term sub-mesoscale eddy because oceanographers define the dividing line between mesoscale and sub-mesoscale eddies in terms of the baroclinic Rossby radius of deformation, which depends on latitude and oceanographic parameters (see, e.g., Chelton et al., 1998) and thus has not a fixed length.

Small-scale oceanic eddies having horizontal scales below 50 km have first been observed from space on sunglint images (Scully-Power, 1986; Soules, 1970), and later also on synthetic aperture radar (SAR) images (DiGiacomo & Holt, 2001; Fu & Holt, 1983; Ivanov & Ginzburg, 2002; Johannessen et al., 1993, 1996; Karimova, 2012; Munk et al., 2000; Yamaguchi & Kawamura, 2009). Small-scale eddies are much less understood than mesoscale eddies, which can be modeled quite well by present-day global ocean models which have a resolution of the order of 10 km (Capet et al., 2008; Le Galloudec et al., 2008; Maltrud & McClean, 2005). However, small-scale eddies cannot be modeled by using traditional quasi-geostrophic theory which applies to mesoscale eddies (Thomas et al., 2008). By using high-resolution simulations, Eldevik and Dysthe (2002) show that small-scale eddies produced by the instability of a geostrophic surface flow are restricted to the very upper ocean and that they are a source of kinetic energy for the larger scale flow. Like mesoscale eddies, also small-scale eddies can be generated by several processes, like interaction of large-scale currents with the bottom topography, islands or headlands, by barotropic or baroclinic instability of currents and fronts, or by atmospheric forcing (vorticity input from wind stress). Furthermore, also small-scale eddies can transfer heat, salt, trace gases, nutrients, and chlorophyll-a (CHL) across frontal zones (see, e.g., Morrow et al., 2003; Olson, 1991). In particular, they also can transport nutrients from upwelling regions into oligotrophic ocean regions causing enhanced CHL concentration there.

Small-scale eddies are particularly often encountered in enclosed and semi-enclosed seas, like the Caspian Sea, the Mediterranean Sea, the Black Sea, and the Baltic Sea. In a recent study, Karimova (2012) has analyzed over 2000 SAR images acquired by the European Remote Satellites ERS-1 and ERS-2 and the European Envisat satellite over the Baltic, the Black and the Caspian seas in 2009–2010. She detected on them more than 14,000 radar signatures of vortical structures with diameters between 1 and 75 km. About 99% of them had diameters in the range of 1–20 km and 98% had a cyclonic rotation.

In this paper we report about a single small-scale eddy which was generated at the headland of Cap-Vert off the coast of Senegal (14° 45′ N, 17° 31′ W) following a sudden freshening of the trade winds. Due to favorable cloud conditions, we were able to track the time evolution of the eddy for 31 days by satellite images acquired in the visible/infrared bands. Furthermore, during this period the eddy was also imaged by a space-borne SAR. The satellite data we are using are from the MODIS (Moderate Resolution Imaging Spectroradiometer) sensor onboard the American Aqua satellite, the AVHHR (Advanced Very High Resolution Radiometer) sensor onboard the European MetOp satellite, and the Advanced SAR (ASAR) onboard the European Envisat satellite. While MODIS and AVHRR are optical/infrared sensors, which can retrieve information on sea surface temperature (SST) and CHL concentration only over oceanic areas with no or little cloud coverage, the SAR is an active microwave instrument which can take images independently of cloud coverage and the time of the day. SST and CHL maps are derived from these images which show the westward motion of the eddy from the Senegal upwelling region into the open North Atlantic Ocean. During the 31 days of satellite observations, the eddy moved 200 km westward thereby carrying nutrients from the upwelling region into the oligotrophic North Atlantic, where it caused enhanced CHL concentration. Furthermore, we recorded the movement of the eddy by a satellite-tracked surface drifter. To our knowledge, this is the first time where a small-scale eddy moving from an upwelling region into an oligotrophic ocean has been tracked by its SST, CHL, and radar signatures over such a long time by using simultaneously acquired satellite and surface drifter data.

The paper is organized as follows: In Section 2 we give a short summary of the importance of small-scale eddies on the redistribution of heat, nutrients, and CHL in the ocean. Sections 3–6 are devoted to the study of a small-scale eddy generated around 23 October 2011 at the headland of Cap-Vert. In Section 3 we present simulations carried out with the Mercator assimilation model showing how the small-scale eddy was generated by atmospheric forcing caused by freshening of the trade winds. In Section 4 we present data of a satellite-tracked surface drifter deployed in the eddy and derive from them parameters describing characteristics of the eddy. In Section 5 we present SST and CHL maps showing the path and the evolution of the eddy on its way from the generation region into the Atlantic. In Section 6 we present three SAR images showing radar signatures of the eddy and discuss what information they contain. In Section 7 we discuss and summarize the results, and in Section 8 we give an outlook on how to monitor small-scale eddies from space in the future.

2. Small-scale eddies in the ocean

High-resolution satellite images and oceanographic field measurements have revealed intense, transient, small-scale motions associated with eddy activity in many parts of the ocean (Lévy et al., 2010) and in lakes (Karimova, 2012). Typically, these motions with horizontal scales of the order of 10 km are difficult to observe by in-situ methods (D'Asaro, 1988; Kaz'min & Kuz'mina, 1990; Marullo et al., 1985; McWilliams, 1985) and difficult to model. By comparing models of different horizontal resolutions, including an extremely high-resolution model of 1/54°, Lévy et al. (2010) have shown that with increasing resolution smaller and smaller eddies are generated. The small-scale flow field, which is largely ageostrophic, strongly affects the large-scale ocean circulation.

Mesoscale eddies as well as small-scale eddies are instrumental in transporting cold water and nutrients from upwelling regions into oligotrophic ocean regions. Although more than 30 years ago, Gower et al. (1980) have pointed out that phytoplankton patchiness is linked to mesoscale eddies, it has been realized only recently that eddies play a key role in the variability of the CHL distribution in the World's ocean (Lathuilière et al., 2011; Williams, 2011). Chelton et al. (2011b) state that most of the variability of CHL distribution results from redistribution of CHL caused by advection with the mesoscale flow field and not from changes in the local phytoplankton growth. At the beginning of their life, eddies cause horizontal and vertical transfers of heat and nutrients as they form in regions of strongly sloping density surfaces. At a later stage, they often move far away from their region of origin as coherent structures. Finally, they die and release their properties to the environment. Often the CHL distribution associated with eddies consists of dipoles with maximum and minimum CHL values outside of the eddy cores (Chelton et al., 2011a,b). However, also monopoles, where the positive or negative CHL anomalies are located in the center of the eddy, are frequently observed on satellite images. In cyclonic eddies, whose isopycnal doming allows nutrients to reach the euphotic zone, maximum CHL concentration is usually located in the center. This paper deals with this kind of eddies. Occasionally, also large-scale eddies with diameters of the order of 600 km have been observed which transport nutrients and CHL from a coastal area hundreds of kilometers away into oligotrophic regions (Lin et al., 2010).

Thus cyclonic eddies contribute to stimulate phytoplankton growth and transport phytoplankton from nutrient-rich to nutrient-poor regions. They are also oasis for higher trophic marine life, since they provide optimal conditions for enriched feeding in the open ocean (Atwood et al., 2010; Godø et al., 2012). On the other hand, mesoscale eddies are also responsible for the reduction of the biological activity in coastal upwelling regions since they transport nutrient-rich water away from the coast (Gruber et al., 2011).

Most of the literature dealing with the transport of nutrients and CHL by eddies from upwelling into oligotrophic regions refer to mesoscale eddies with diameters above 50 km (Falkowski et al., 1991; Greenwood et al., 2007; Heywood & Priddle, 1987; Ladd et al., 2009; Levy et al., 2001; Lin et al., 2010; Perissinotto & Rae, 1990). However, we anticipate that the same transport mechanism applies also to small-scale eddies with diameters below 50 km. Due to the reasons listed above, there exist only relatively few papers dealing with measurements of small-scale eddies; among them are the papers by D'Asaro (1988), Bassin et al. (2005), DiGiacomo and Holt (2001), and Kasajima et al. (2006). In the first paper, small-scale eddies were investigated in the Beaufort Sea by using helicopter-borne expendable current profiler and conductivity–temperature–depth (CTD) data, in the second paper they were studied in the Southern California Bight by using synthetic aperture radar (SAR) images as well as surface drifter and mooring data, in the third paper they were studied in the Southern California Bight by using shore-based HF radar data, and in the fourth paper they were studied in the Greenland Sea by using hydrography, chemical tracer, and velocity profiler data.

In this paper we study a small-scale eddy by using multi-sensor satellite data and data from a surface drifter moving with the eddy. Like for larger scale eddies, also this eddy constitutes a source of nutrient anomaly which is transported over long distances, in this case from the upwelling area of the Senegalese coast westward into the open North Atlantic Ocean. Thus this small-scale eddy served as a vehicle to transport plankton into the oligotrophic East Atlantic Ocean.

3. Generation of the small-scale eddy at Cap-Vert

The small-scale eddy analyzed in this paper has its origin in the upwelling area off the coast of Senegal in West Africa. The coast of West Africa between 12° and 25°N is a well-known upwelling area, located in the large marine system influenced by the Canary current and driven by the trade winds. Between 20° and 25°N, upwelling is a permanent phenomenon, but between 11° and 20°N it occurs only in winter and spring (Demarcq, 1998). Since the eddy investigated in this paper originated from the coastal waters near Cap-Vert, we suspect that the headland of Cap-Vert played a key role in its generation. It is well known from other parts of the World's ocean that headlands are birthplaces of eddies (Davies et al., 1995; Denniss et al., 1994; Munchow, 2000; Murdoch, 1989; Pattiaratchi et al., 1987; Signell & Geyer, 1991). Also DiGiacomo and Holt (2001) noted that most of the small-scale eddies in the Southern California Bight are observed in close proximity of islands and headlands, which suggests that they are topographically generated. Since eddy generation at Cap-Vert does not occur on a regular basis, it must have been caused by a sudden change in environmental conditions. One would expect that the most likely cause was a wind burst directed southward along the coast which caused an increase of the surface flow. This was indeed the case as revealed by the four wind maps depicted in Fig. 1. The maps show near-sea surface wind fields provided by the National Climatic Data Center (NCDC) of the National Oceanic and Atmospheric Administration (NOAA), which generates them from a blend of satellite data,

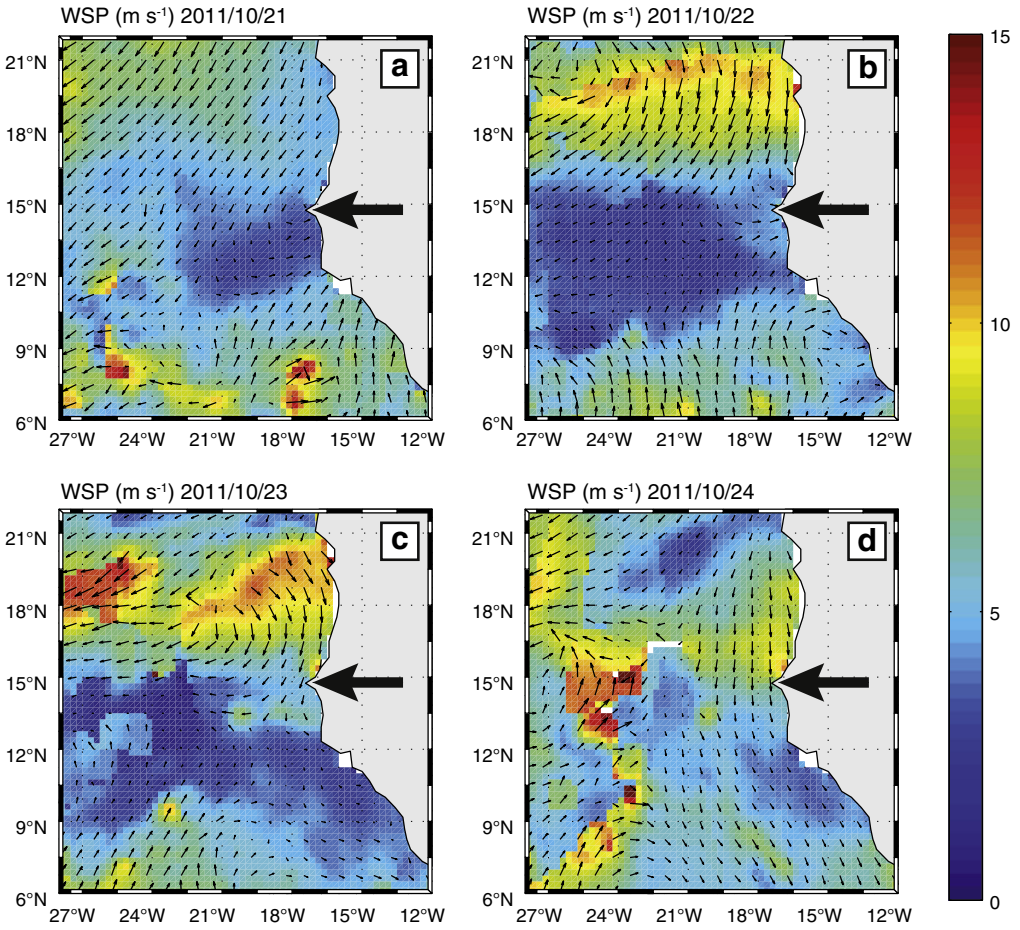

Fig. 1. Near sea surface wind fields provided by the National Climatic Data Center of NOAA generated from a blend of satellite data for 00 UTC on (a) 21 October, (b) 22 October, (c) 23 October, and (d) 24 October 2011. a shows a wind field typical for this time of the year and Fig. 1b,c, and d shows the time evolution of the wind burst advancing southward along the coast of West Africa toward Cap-Vert (marked by an arrow).

including data from the scatterometer ASCAT onboard the European MetOp satellite (Zhang et al., 2006, http://www.ncdc.noaa.gov/oa/rsad/air-sea/seawinds.html). The four wind maps, which all refer to 00 UTC, show the time evolution of the wind field which caused the generation of the eddy. Fig. 1a shows the wind field on 21 October 2011 before the onset of the wind burst and Fig. 1b,c, and d the wind fields on 22, 23 and 24 October, respectively, showing different stages of the time evolution of the wind burst approaching Cap-Vert. On 23 October at 00 UTC (Fig. 1c) the maximum wind speed was 11 m s^{-1}, and on 24 October, when the wind burst had reached Cap-Vert, the wind speed had dropped to 9 m s^{-1} (Fig. 1d).

In order to investigate the ocean circulation forced by the wind burst, we have analyzed simulations performed with the "Mercator Global Operational System PSY2V4R2" (Lellouche et al., 2012). This model assimilates sea level anomalies, SST, and temperature/salinity (T/S) profiles. It is forced by wind and surface heat and freshwater fluxes provided by the European Centre for Medium-Range Weather Forecasts (ECMWF). It has a horizontal resolution of 1/12° (9 km at the equator and 3 km at 70°N) and thus is well suited to study the generation and propagation of mesoscale eddies of scales above 50 km, but cannot simulate small-scale eddy dynamics.

However, here we have used the Mercator model only to shed light on the onset of a southward wind-induced coastal current which we suspect to be responsible for the generation of the small-scale eddy at the headland of Cap-Vert. In Fig. 2a–c the surface current fields (represented by arrows) superimposed on the SST field (represented by colors) simulated by the Mercator model for 00 UTC on 23, 27, and 31 October 2011, respectively, are depicted. On 23 October (Fig. 2a), the flow at the approaches to Cap-Vert is dominated by northward flow associated with high SST values within the region. Four days later (Fig. 2b), a strong southward directed surface current, forced by the wind burst, dominated the coastal region north of Cap-Vert.

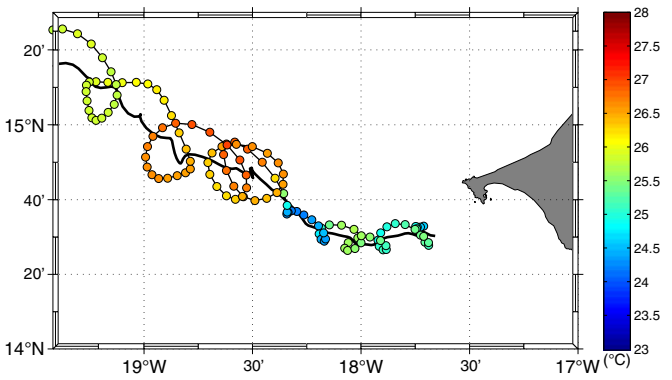

Fig. 3. Time series of the position of the satellite-tracked surface drifter from 29 October to 27 November 2011. The colors in the circles denote the water temperature at a depth of 20–30 cm below the sea surface. The black line denotes the motion of the center of the eddy.

Accordingly, upwelling occurred which is clearly visible as a coastal band of reduced SST on the SST map depicted in Fig. 2b. Note that maximum surface velocities are centered next to Cap-Vert, where also the SST is reduced. The map depicted in Fig. 2c shows that cold water has intruded the area southwest of Cap-Vert and that south of Cap-Vert warm water was flowing northward along the coast. This flow forms, together with the southward flow further west, a cyclonic flow pattern. Such a recirculation of water behind an obstacle is typical for eddy generation by flow separation. The onset of the along-shore flow on 23 October can also be seen on the plot depicted in Fig. 2d, which shows how the simulated SST (black curve) and along-shore surface current (red curve) varied with time. The plot applies for the grid point 15.39°N,

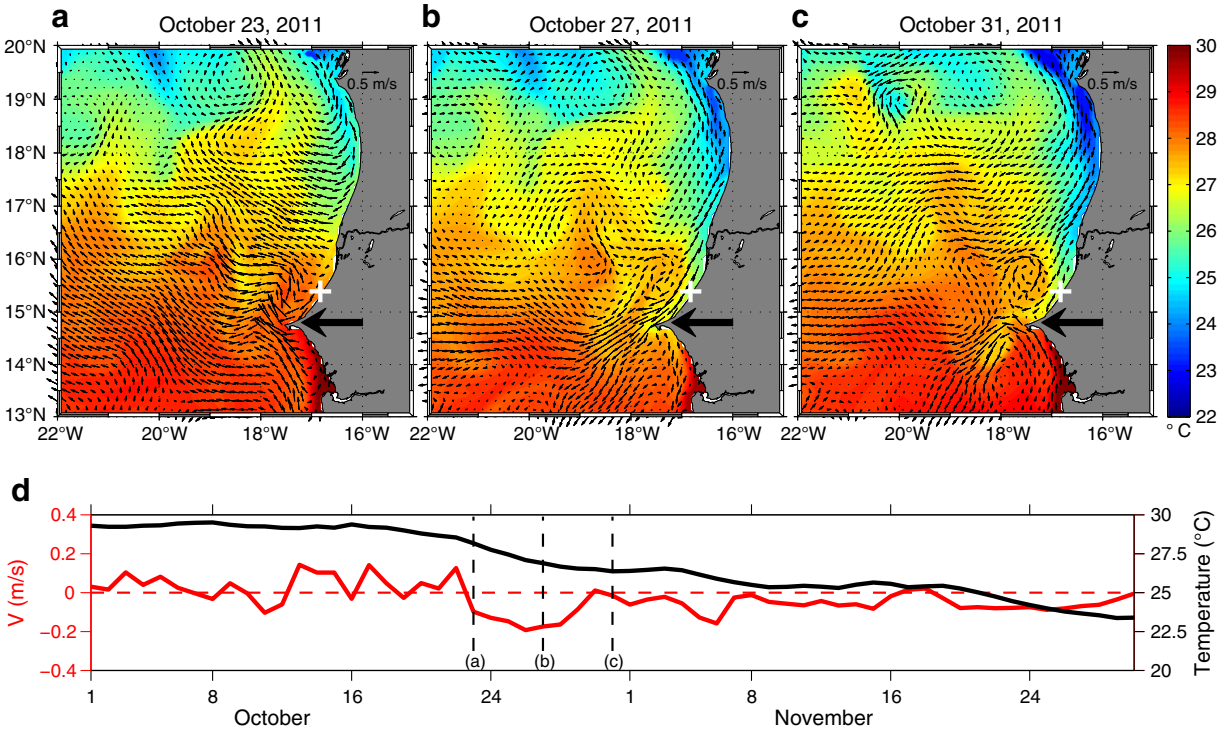

Fig. 2. Upper panels a, b, and c: simulated sea surface current field (black arrows) superimposed on the simulated SST field (colors) calculated by the Mercator model for 00 UTC on (a) 23 October, (b) 27 October, and (c) 31 October 2011, respectively. The maps show the surface current fields before and after the onset of the enhanced surface flow caused by the wind burst. Panel c shows that cold water has intruded the area southwest of Cap-Vert (marked by a thick black arrow) and that south of Cap-Vert warm water is flowing northward along the coast. This cyclonic circulation pattern suggests that flow separation has taken place. Lower panel d: time series of the sea surface temperature (black curve) and the along-shore surface current (red curve) at the grid point 15.39°N, 16.83°W, which is the grid point next to the coast slightly north of Cap-Vert (marked by a white plus sign in panels a, b, and c), simulated by the Mercator model. It shows the development of a strong southwestward near coastal current starting on 23 October 2011. The dashed lines mark the times of the simulations depicted in panels a, b, and c.

16.83°W, which is the grid point next to the coast slightly north of Cap-Vert (see Fig. 2). The three dashed lines inserted in Fig. 2d mark the times at which the simulations shown in Fig. 2a–c were carried out. The plot shows the onset of a strong near coastal current on 23 October (marked by the first dashed line from the left) and a drop in SST due to upwelling and southward advection of colder water masses. We suspect that flow separation at Cap-Vert, as visible in the simulated flow field depicted in Fig. 2b, represents the initial stage of the highly nonlinear eddy generation process. However, the model is not capable to reproduce the cyclogenesis in detail and cannot describe the generation of highly nonlinear eddies. But the model is capable of describing the upwelling induced by the northerly wind burst and the environment in which the small-scale eddy was generated.

4. Satellite-tracked surface drifter data

A surface drifter was deployed on 29 October 2011 in the core of the eddy at 17°43′W, 14°33′N southwest of Dakar. The drifter is a mini Surface Velocity Program (SVP) drifter manufactured by Clearwater Instrumentation, Watertown, MA, USA (Lumpkin & Pazos, 2007). It is equipped with an SST sensor and a pressure sensor for monitoring the vertical position of the drogue centered at a nominal depth of 15 m. The surface drifter was tracked by the Argos Data Collection and Location System with horizontal position accuracy better than 1500 m. The drifter position data were first edited for spikes and outliers and then linearly interpolated at regular 2-h intervals by using the kriging technique (Hansen & Poulain, 1996). The interpolated positions were low-pass filtered by using a Hamming filter (cut-off period at 36 h) in order to remove higher frequency current components and were finally sub-sampled at 6-h intervals. Velocity components were then estimated from centered finite differences of 6-h sub-sampled data. The trajectory of the drifter between 29 October and 27 November 2011 is depicted in Fig. 3. The colors in the circles denote water temperature measured by the drifter at a depth of 20–30 cm below the sea surface. In order to extract the properties of the eddy from this time series, the wavelet ridge analysis developed by Lilly and Gascard (2006) and Lilly et al. (2011) has been applied. In this analysis the time series is decomposed in a time-varying elliptical signal and a residual. The elliptical signal is associated with the intrinsic eddy rotation, and the residual represents the eddy translation (thick solid line in Fig. 3). Lilly and Gascard (2006) provided with their paper a software package, written in Matlab, for performing the analyses and generating plots (http://www.jmlilly.net).

Based on such flow decomposition, the mean azimuthal velocity V_m and the mean radius R_m of the drifter rotation around the eddy core

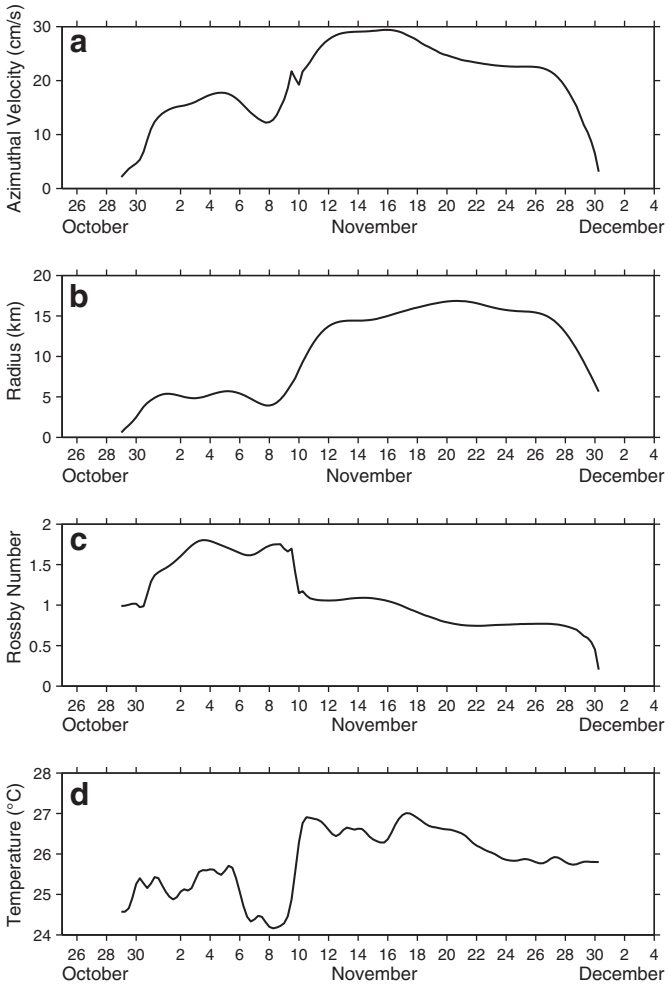

Fig. 4. (a) Azimuthal velocity of the drifter around the eddy core, (b) radius of the drifter trajectory, (c) Rossby number of the eddy, and (d) water temperature at a depth of 20–30 cm below the sea surface as function of time as obtained from the surface drifter data.

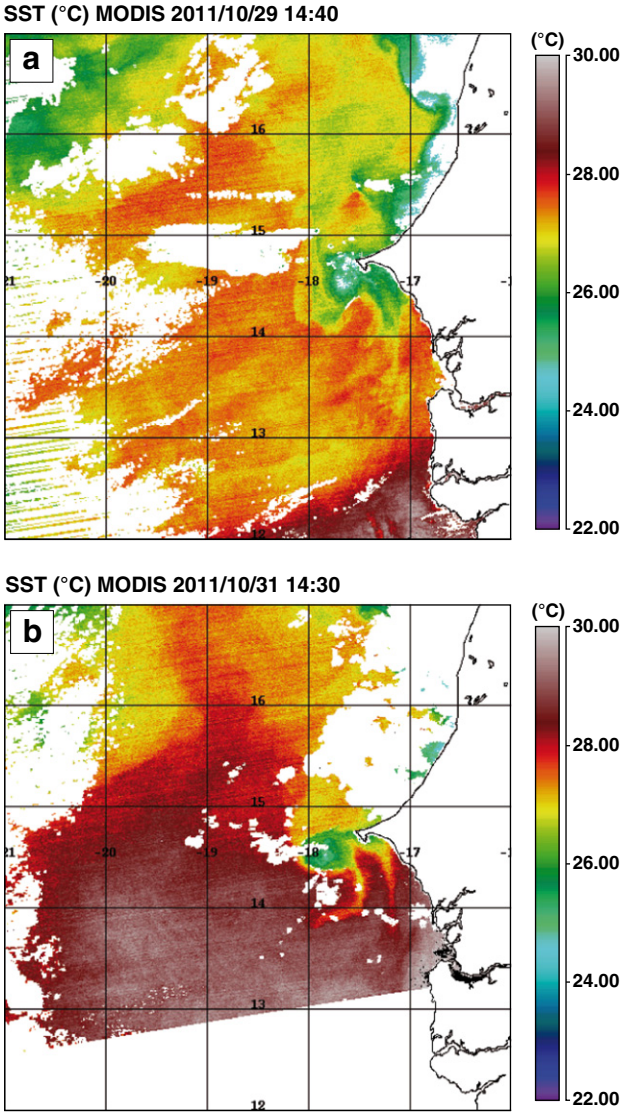

Fig. 5. SST retrieved from MODIS data acquired (a) at 1440 UTC on 29 October 2011 and (b) at 1430 UTC on 31 October 2011. The white areas are land (on the right), clouds where no SST could be retrieved, or regions where no data were acquired.

have been estimated. We used these values to calculate the eddy Rossby number:

$$Ro = V_m/(f * R_m) \quad (1)$$

where f is the Coriolis parameter.

These parameters (V_m, Rm, and Ro) as extracted from the time series depicted in Fig. 3 are plotted in Fig. 4. Furthermore, also the water temperature as measured by the surface drifter is plotted as a function of time in Fig. 4d. Fig. 3 shows that the eddy propagated in a northwestward direction. According to the linear theory, a cyclonic eddy should propagate westward on a beta-plane (see e.g., Cushman-Roisin et al., 1990; Korotaev & Fedotov, 1994; Lam & Dritschel, 2001). However, cyclonic eddies tracked in a nonlinear quasi-geostrophic model show a poleward deflection from purely westward shift that was found to be consistent with satellite observations (Early et al., 2011) and which is also observed for the present eddy.

After an initial stage, we observe two different phases of the drifter movements around the eddy. During the week from 1 to 8 November, the drifter rotated close to the eddy center (about 5 km apart, see Fig. 4b). Accordingly, the measured water temperature was relatively low, which is typical for upwelled water located in the core of the eddy. After a short transition phase, during which the drifter rapidly departed from the eddy center, a second, almost stationary stage lasting for about 2 weeks followed (mean radius about 15 km, see Fig. 4b). The water encountered by the drifter at this distance from the eddy core was substantially warmer and barely exhibited eddy core properties. More importantly, the eddy as measured by the drifter was highly nonlinear as inferred from the value of Rossby number (Ro) which exceeded 1 (Fig. 4c). The Rossby number stayed above 1 until 19 November and did not drop below 0.5 until 29 November. Note, however, that the Ro estimation crucially depends on the assumed structure of the azimuthal velocity of the eddy (Rubino & Brandt, 2003; Rubino et al., 1998). For comparison, typical Rossby numbers of known mesoscale oceanic eddies, like, e.g., Gulf Stream rings, rarely exceed 0.2. Hence the observed eddy, particularly during its initial stage, was extremely nonlinear with a maximum Rossby number of Ro = 1.8. Its nonlinear terms overwhelmed the Coriolis term in the momentum balance.

5. Sea surface temperature and chlorophyll-a maps

Figs. 5–7 show the time evolution of the small-scale eddy between 29 October and 28 November 2011 in the form of SST and CHL maps retrieved from Aqua MODIS data. The SST maps show sea surface signatures of the eddy, while the CHL maps show the CHL distribution in the upper layer of the ocean. These maps show that the cyclonic eddy drifted first southwestward and then northwestward into the open Atlantic. Sea surface signatures of the cold eddy are visible on all SST

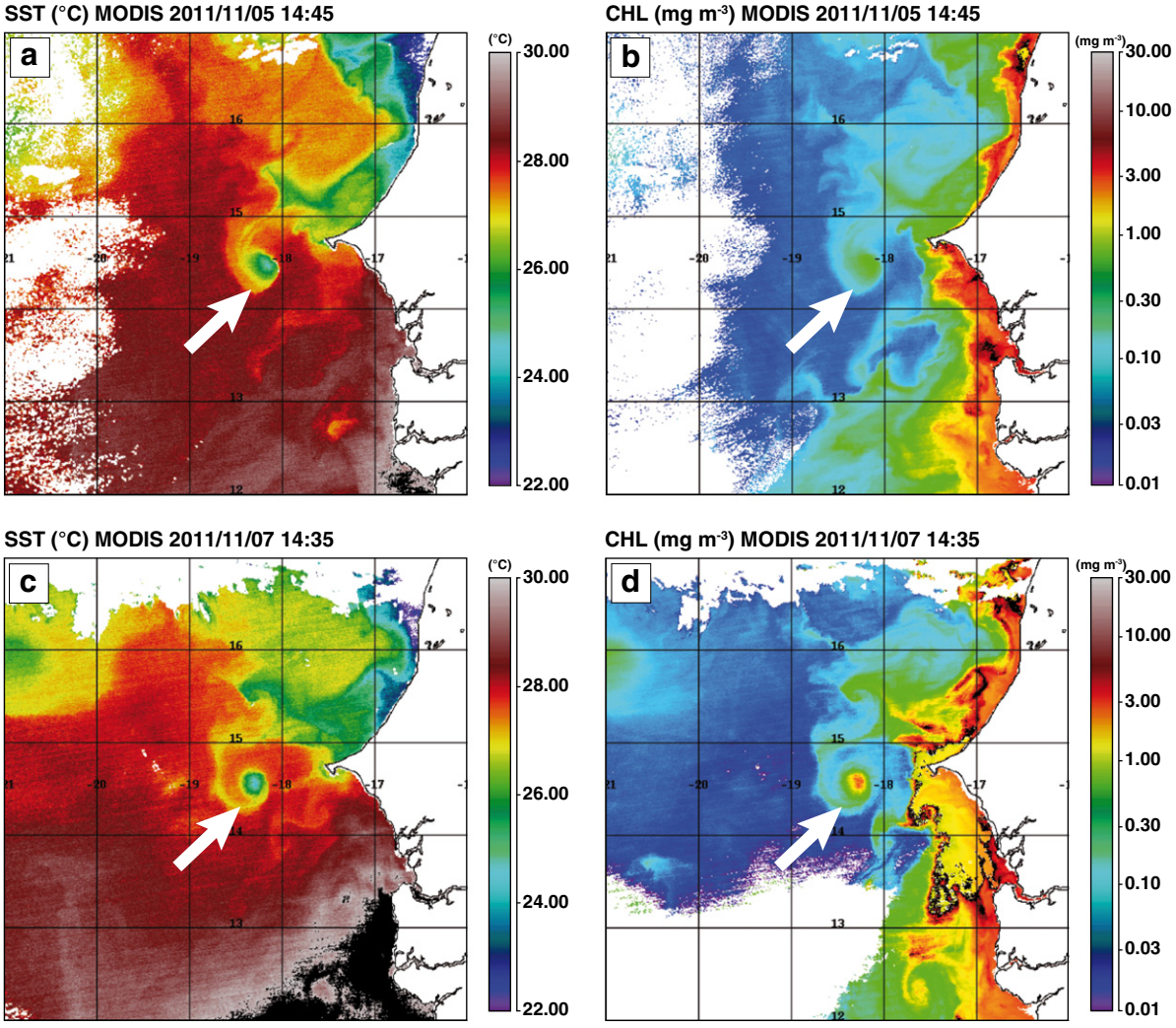

Fig. 6. Maps of the SST in degrees C and of the chlorophyll-a (CHL) concentration in mg/m^3 retrieved from MODIS data. Upper maps: at 1445 UTC on 5 November 2011. Lower maps: at 1435 UTC on 7 November 2011. The arrows point to the SST and CHL signatures of the small-scale eddy.

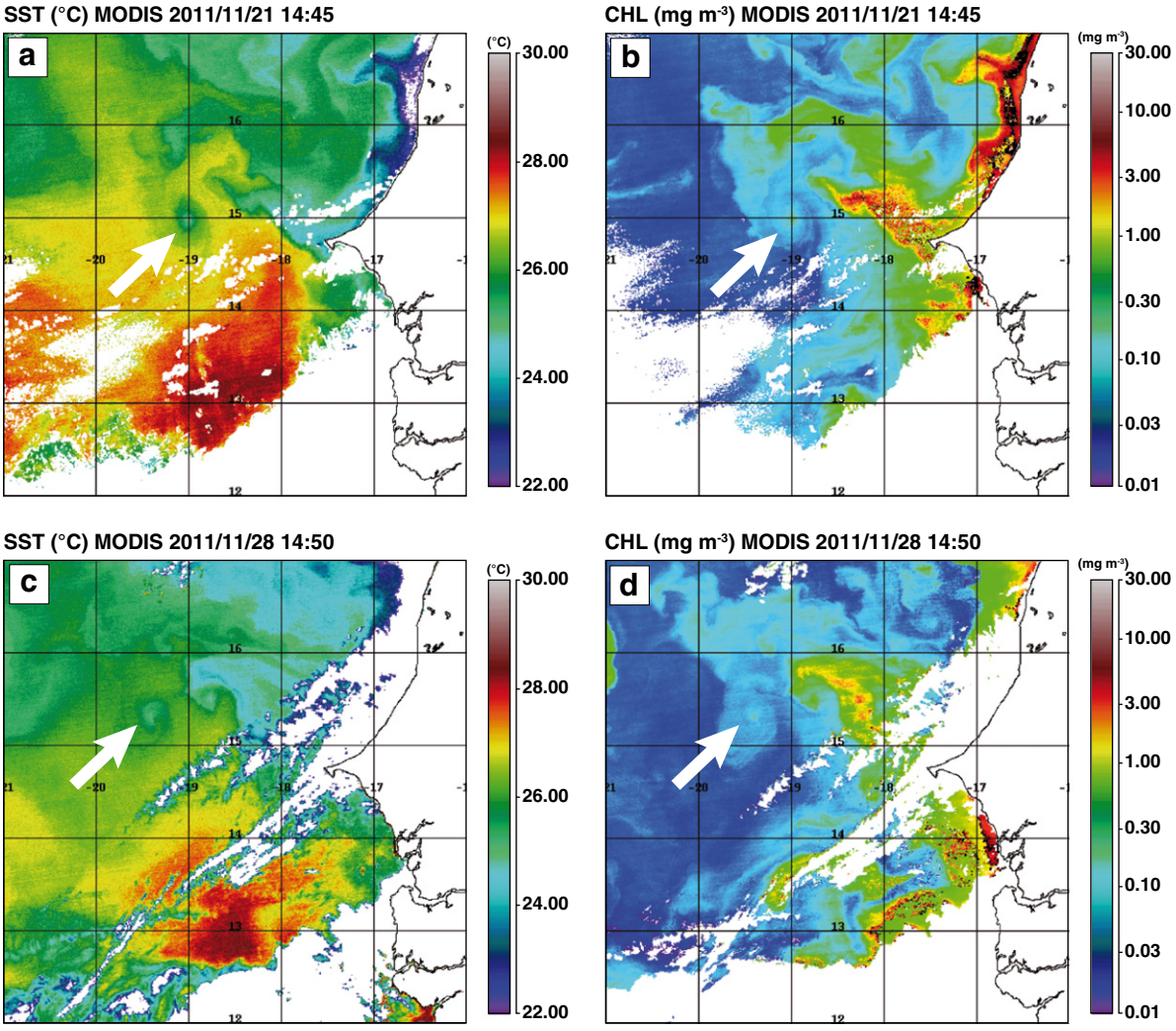

Fig. 7. Same as Fig. 6, but at 1445 UTC on 21 November 2011 (upper maps) and at 1450 UTC on 28 November 2011 (lower maps).

maps. The SST maps depicted in the lower left panel of Fig. 6 and in 8 show spiral arms emanating from the core of the eddy which are warmer than the core of the eddy, but still about 1.0–1.5 °C cooler than the surrounding waters.

When comparing the SST and CHL maps in Figs. 6 and 7, we see that the centers of the patches with strongly reduced SST (about 2 °C colder than the surrounding waters) and with strongly enhanced CHL concentration (about 3 mg m^{-3} higher) coincide. While the diameter of the core of the eddy in the SST maps is estimated to vary between 15 and 30 km, the diameter of the eddy in the CHL maps is more difficult to estimate. In these maps the patch of strongly enhanced CHL distribution is surrounded by a broad band with medium enhanced CHL (about 1 mg m^{-3}). The SST maps (acquired during daytime, see captions to Figs. 6 and 7) show that the maximum reduction of the SST in the core of the eddy relative to the surrounding waters is about 2.5 °C. However, this does not necessarily correspond to the maximum temperature difference between the upwelled water in the eddy core and the surrounding water. Typically, the SST measured during night time over the eddy is lower than the SST measured during day time and hence more representative for the true temperature of the upwelled water. Wang and Tang (2010) have studied this phenomenon and argued that, during daytime, absorption of solar radiation is enhanced by the presence of phytoplankton, which leads to higher daytime SST over phytoplankton bloom areas. These authors have estimated that the difference between daytime and nighttime SST depends on the CHL concentration and is of the order of 1 °C for a concentration of 3 mg m^{-3}. In Fig. 8 two pairs of SST maps are shown that were derived from MetOp AVHRR data acquired shortly before noon (local time is equal to UTC) and during the night. They clearly show that at daytime the SST has increased everywhere due to diurnal warming, but they also show that this increase is stronger in the eddy area, which is agreement with the observations of Wang and Tang (2010).

6. Synthetic aperture radar images

In Figs. 9a–11a three SAR images are depicted, which were acquired between 30 October and 2 November 2011 by the ASAR onboard the Envisat satellite (http://envisat.esa.int/handbooks/asar/). Two of them (Figs. 9a and 11a) were acquired in the Global Mode (GM) with a resolution of 1 km (500 m pixel spacing) and one (Fig. 10a) in the Wide Swath Mode (WSM) with a resolution of 150 m (75 m pixel spacing). All SAR images show radar signatures of the small-scale eddy in the form of patches of reduced image intensity. The SAR images are calibrated with respect to normalized radar cross section (NRCS), which is a measure of the backscattered radar power (see, e.g., Valenzuela, 1978). Thus the SAR images represent NRCS maps. From these SAR images we have retrieved near-surface wind fields by using the CMOD4 wind scatterometer model (Stoffelen & Anderson, 1997) and the wind directions from the National Center of Environmental

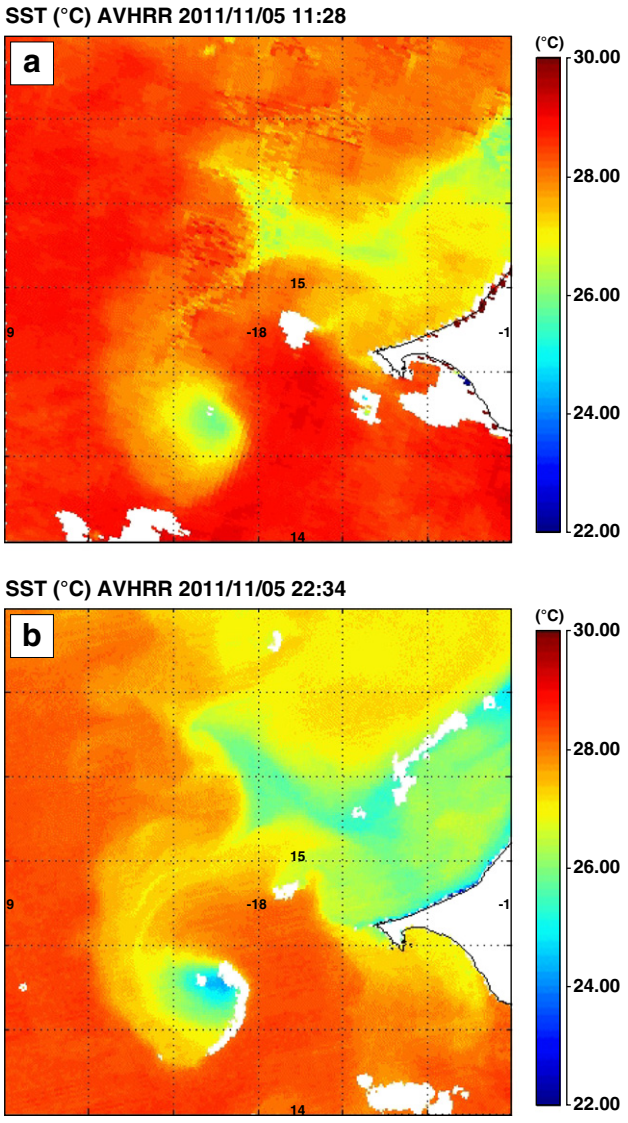

Fig. 8. Maps of the SST retrieved from MetOp AVHRR data acquired (a) at 1128 UTC on 5 November 2011 and (b) at 2234 UTC on the same day. Note that during the night (b) the core of the eddy is about 0.5 °C colder than during daytime.

Predictions (NCEP) model (Alpers et al., 2011; Sikora et al., 2006). The wind fields are depicted in Figs. 9c–11c.

Not only quantitative information on near-surface wind fields can be extracted from SAR images, but also information on eddies and upwelled cold water via the reduction of the NRCS. For this purpose we have made NRCS scans along transects through the radar signatures of the small-scale eddy visible on all three SAR images These scans are shown in Figs. 9b–11b. We have refrained from normalizing the plots, i.e., we have not corrected them for the incidence angle dependence of the NRCS, which is of no relevance for this investigation. In order to render the NRCS reductions better visible on the plots, we have chosen different NRCS dB scales in the plots. The plots have been generated from the SAR images by digitizing them with a 500 m pixel spacing and by averaging over 5 pixels by using a mean filter. Inspection of the plots depicted in Figs. 9b–11b shows that the dark patches visible on the SAR images give rise to dips in the NRCS curves. Although the curves exhibit large variations, estimates of the maximum reduction of the NRCS over the eddy can be obtained. On the NRCS plot depicted in Figs. 9b–11b, the measured reductions are estimated to be 3 dB, 13 dB, and 10 dB, respectively. Maximum NRCS reduction was found not in the eddy core but near the southwestern rim of the eddy (cf. Figs. 5b and 10).

There are two mechanisms that can cause reductions of the NRCS over cold eddies. Both of them are associated with damping of the short-scale sea surface roughness. Short-scale roughness denotes in this context short surface waves with wavelengths in the centimeter to the decimeter range which, according to the Bragg scattering theory, determine the radar backscattering (Valenzuela, 1978). The damping can be caused by 1) surface films floating on the sea surface or by 2) a change of the stability of the air–sea interface due to upwelled cold water. In general, the reduction of the NRCS due to surface films is much larger (typically 6 and 15 dB) than that due to the change of the stability of the air–sea interface (typically 0.5–3.0 dB).

6.1. Reduction of the NRCS by surface films

As shown in Section 5, the small-scale eddy analyzed in this paper is associated with a high CHL concentration and thus with high biological productivity. Unfortunately there are no CHL maps available from the early stages of eddy development, i.e., before 5 November 2011. However, the maximum NRCS reduction near the southwestern rim found during the early stage of eddy development, is most likely connected to enhanced nutrient supply in the frontal region of the cold eddy. Such a supply of nutrients to ocean eddies was found to be affected by submesoscale processes that act along the periphery of eddies and can induce vertical velocities several times larger than those associated with other processes like e.g., eddy–wind interactions (Mahadevan et al., 2008). Therefore we expect that much surface active material is secreted by the biota near the rim of the eddy, which ascends to the sea surface and forms there surface films. These so called biogenic surface films are usually only mono-molecular layers, but they can damp the short-scale ocean waves as strongly as mineral oil films (Alpers & Espedal, 2004; Wismann et al., 1998). According to the Bragg scattering theory (Valenzuela, 1978), damping of these waves causes a reduction of the NRCS. There exist only few measurements of the reduction of the C-band NRCS by biogenic surface films (Espedal et al., 1998; Huehnerfuss et al., 1996), which show that this reduction is quite variable, depending on wind speed and type of biogenic surface films. The measurements show that the reduction is typically larger than 6 dB in the wind speed range from 2 to 6 m s^{-1}. Even NRCS reductions of 17 dB have been measured (Espedal et al., 1998). At wind speeds larger than about 8 m s^{-1}, the surface films disappear from the sea surface because they get entrained in the underlying water by wave breaking (Alpers & Espedal, 2004; Romano & Marquet, 1991) and thus cannot contribute to the NRCS reduction anymore. On the other hand, at wind speeds below 1–2 m s^{-1}, no short surface waves ("Bragg waves") are generated by the wind that can cause radar backscattering. Thus, also in this case, the presence of surface films cannot reduce the NRCS anymore.

6.2. Reduction of the NRCS by change of the stability of the air–sea interface

Usually the air–sea interface is neutrally stable, which is the case when the water and air temperature are equal. However, when the water temperature becomes lower than the air temperature, the air–sea interface becomes stable. As a result the friction velocity (or wind stress) decreases and thus less short waves are generated (see, e.g., Kozlov et al., 2012; Large & Pond, 1981). Measurements of the reduction of the NRCS as a function of air–sea temperature difference were carried out by Keller et al. (1989) with a C band scatterometer mounted on a platform in the North Sea. The data show that the NRCS decreases with increasing air–sea temperature difference approximately by 1.2 dB/°C for wind speeds between 6 and 7 m s^{-1}, by 1.0 dB/°C for wind speeds between 8 and 9 m s^{-1}, and by 0.75 dB/°C for wind speeds between 11 and 12 m s^{-1}. Clemente-Colon and Yan (1999)

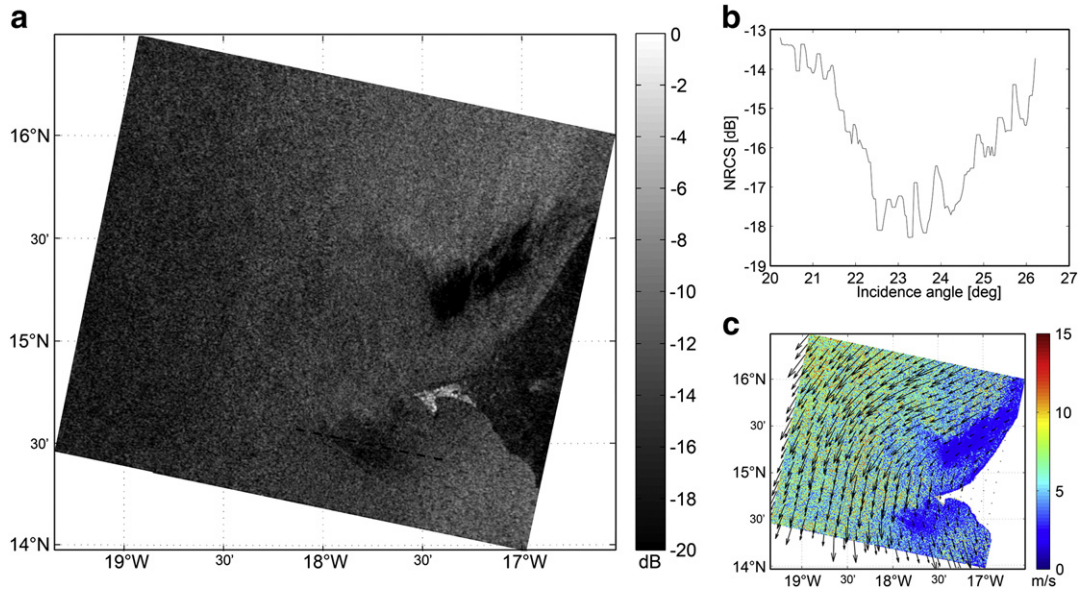

Fig. 9. (a) Section of an ASAR image acquired in the Global Mode (GM) at 1112 UTC on 30 October 2011 during a descending satellite pass. Cap-Vert, which has the form of a hook, is visible in the right-hand section of the image. The patch of slightly reduced image intensity southwest of Cap-Vert is the radar signature of the small-scale eddy, and the patch of strongly reduced image intensity (black patch) northeast of Cap-Vert the radar signature of an area in the coastal upwelling zone covered by surface films. (b) Variation of the NRCS along the dashed line inserted in the ASAR image. The vertical scale ranges from −19 to −13 dB. The eddy causes a drop of the NRCS of about 3 dB. (c) Near-surface wind field is derived from the ASAR image.

have obtained from their analysis of ERS-2 SAR images acquired over the US Mid-Atlantic coastal ocean in combination with the SST data acquired by the AVHRR sensor onboard NOAA satellites values between 0.5 and 1.0 dB/°C. Given the fact that they did not specify the wind speed range, we consider their values to be compatible with the values measured by Keller et al. (1989). Recently Yang et al. (2011) proposed a new relationship between reduction of the NRCS and the sea–air temperature difference and wind speed. They analyzed Radarsat-1 SAR images in combination with AVHRR SST and buoy data from the National Data Buoy Center and derived the following relationship:

$$\Delta\sigma_0 = 0.105\Delta T + 11.207\left(\Delta T/U^{1.75}\right). \quad (2)$$

Here $\Delta\sigma 0$ denotes the variation of the NRCS in dB, $\Delta T = Tsea - Tair$ is the sea–air temperature difference, and U is the wind speed measured

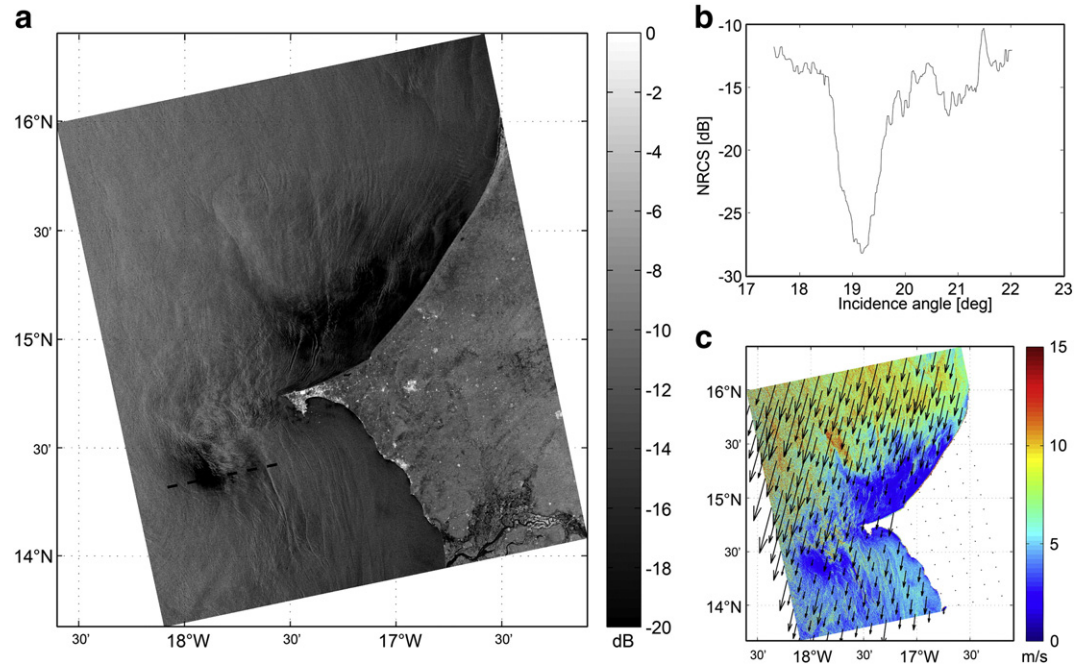

Fig. 10. (a) ASAR image acquired in the Wide Swath Mode (WSM) at 2317 UTC on 31 October 2011 during an ascending satellite pass. The dark patch southwest of Cap-Vert is the radar signature of the small-scale eddy. Maximum NRCS reduction is observed near the southwestern rim of the eddy (cf. Fig. 5b). (b) Variation of the NRCS along the dashed line inserted in the ASAR image. The vertical scale ranges from −30 to −10 dB. The eddy causes a drop of the NRCS of about 13 dB. (c) Near-surface wind field is derived from the ASAR image.

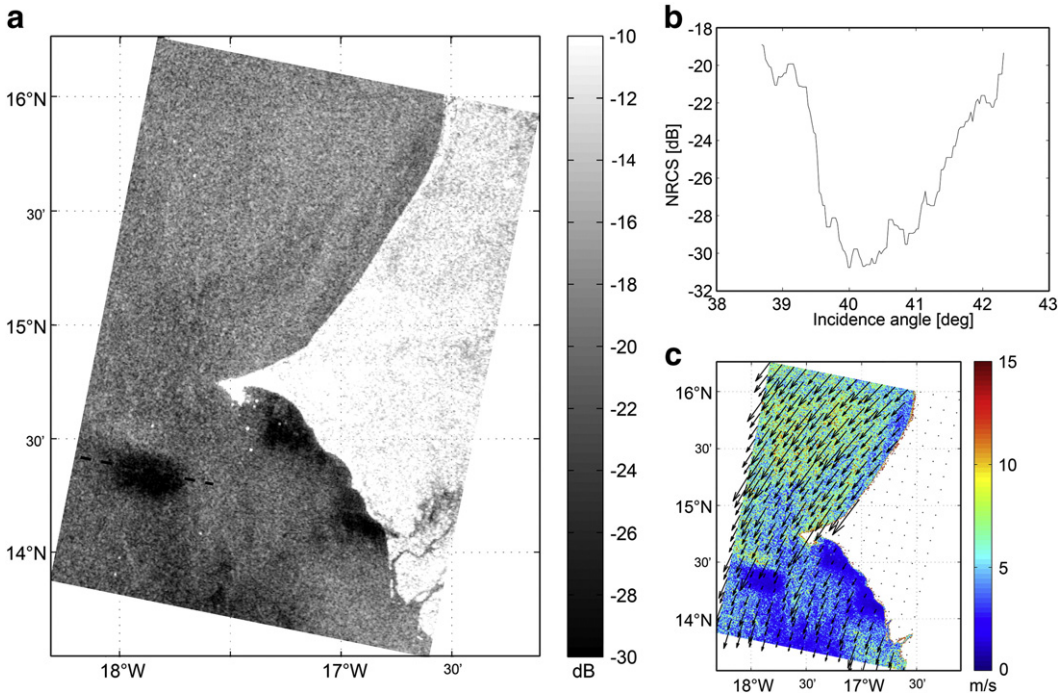

Fig. 11. (a) Section of the ASAR image acquired in the Global Mode (GM) at 1101 UTC on 2 November 2011 during a descending satellite pass. The dark patch southwest of Cap-Vert is the radar signature of the small-scale eddy. (b) Variation of the NRCS along the dashed line inserted in the ASAR image. The vertical scale ranges from −32 to −18 dB. The eddy causes a drop of the NRCS of about 10 dB. (c) Near-surface wind field is derived from the ASAR image.

at a height of 10 m. Note that this relationship applies only for negative values of ΔT.

6.3. Interpretation of the radar signatures of the small-scale eddy

The SST maps derived from the MODIS data show that the difference between the SST in the core of the cold eddy and the SST in the surrounding waters, which we assume to be equal to the air temperature, is about 2.5 °C. When we apply the rate of reduction of the NRCS applicable for the wind speed range of 6–7 m s^{-1}, which, according to Keller et al. (1989) is 1.2 dB/°C, to the SAR image of 30 October (Fig. 9a), we obtain for the reduction of NRCS over the eddy the value of 3 dB, which is just the measured value (Fig. 9b). However, when we apply Eq. (2) and insert the values U = 6 m s^{-1} and ΔT = 2.5 °C, we obtain for the NRCS reduction the value of 1.5 dB. If we assume that the value of 3 dB based on the data of Keller et al. (1989) is correct, than we could conclude that at this early stage of the development of the eddy (on 30 October) the biological activity was so low that no appreciable amount of surface active material ascended to the sea surface to form surface films. In this case we would conclude that the reduction of the NRCS was solely caused by the change of the stability of the air–sea interface from neutrally stable to stable. However, if we assume that the value of 1.5 dB based on the formula of Yang et al. (2011) is correct, then, in addition to the reduction of the NRCS by the change of the stability of the air–sea interface, a small fraction of the eddy area must have been covered with biogenic surface films.

On the other hand, for the two SAR images of 31 October and 2 November (Figs. 10a and 11a), the reductions of the NRCS are 13 and 10 dB, respectively, which clearly points to the presence of biogenic surface films. Subtracting from these values of 3 dB to account for a reduction in NRCS due to cold water, we are left with the NRCS reductions of 10 and 7 dB caused by surface films. These values are well within the range of previously measured reductions of the NRCS by biogenic surface films (Espedal et al., 1998; Huehnerfuss et al., 1996). In addition to the scans through the radar signatures of the eddy, we have also made an NRCS scan through the dark elongated patch northeast of Cap-Vert visible on the ASAR image of 30 October depicted in Fig. 9a. The reduction of the NRCS was measured to be 14 dB, which clearly indicates that this area located northeast of Cap-Vert in the upwelling region is covered by biogenic surface films.

7. Discussion and summary

Near-surface mesoscale eddies having diameters above 100 km can often be detected by conventional radar altimeters of the Topex/Poseidon or Jason type (http://sealevel.jpl.nasa.gov/missions/) via their sea surface height anomalies. However, eddies with diameters typically from few km to 100 km are not resolved by them, but they can be detected from space by high-resolution optical/infrared sensors and by SAR. While optical/infrared sensors can acquire data only when there are no or only few clouds, SAR is capable of providing data independently of cloud coverage and time of the day. However, also SAR has its limitations in imaging small-scale oceanic eddies. The most important ones are 1) the poor coverage of ocean areas by present-day spaceborne SARs and 2) the difficulty to identify unambiguously features (usually dark areas) visible on SAR images as radar signatures of oceanic eddies.

In this paper, we have investigated a small-scale eddy which was tracked for 31 days from its birth place in an upwelling area into an oligotrophic ocean. For this investigation we have used SST, CHL, and sea surface roughness (measured by SAR) data obtained from satellites, and surface drifter data. The eddy was generated at the Cap-Vert headland at the West coast of Africa (Senegal) by enhanced surface flow caused by a wind burst of the trade winds which led to flow separation behind the headland. While moving westward due to the beta effect, the eddy changed its shape, but kept its low SST of 24.5°–25 °C in its center during the entire observation period. This shows that little mixing with the surrounding waters took place. Simultaneously the acquired CHL data show that the eddy transported nutrients from the upwelling region westward into the oligotrophic North Atlantic thus giving rise to enhanced CHL concentration there. Note that the area of lowest SST in the core of the eddy corresponds also to the area of the highest CHL concentration.

In addition to imaging by optical/infrared sensors, the small-scale eddy was also imaged by SAR via the damping of the short-scale surface waves, which causes a reduction of the backscattered radar power or the NRCS. The damping can be caused by 1) surface films floating on the sea surface or by 2) a change of the stability of the air–sea interface due to upwelled cold water. Surface films of biogenic origin are encountered almost always over areas of high biological productivity, i.e., over upwelling areas and over cold eddies. The reduction of the NRCS due to a change of the stability of the air–sea interface above the cold eddies usually causes a weak reduction of the NRCS, at most by 1.2 dB/°C. Since the SST in the center of an eddy, like the one investigated in this paper, is typically 1.5–2.5 °C lower than the SST of the surrounding waters, this implies a maximum reduction of the NRCS by 1.8 to 3 dB. On the other hand, when the reduction is caused by biogenic surface films, the reduction of the NRCS is much larger, typically between 6 and 15 dB.

The SAR image depicted in Fig. 9a shows that, in the very early stage of the development of the eddy, the area above the eddy was not or was only slightly covered with biogenic surface films. This suggests that the phytoplankton growth was not fully developed. However, the SAR images depicted in Figs. 10a and 11a show that, at later stages of the development of the eddy, the southwestern portion of the eddy surface area was covered by biogenic surface films which suggests a high concentration of biota in the eddy. Therefore we suspect that strong CHL growth has taken place after 30 October.

8. Outlook

As stated before, small-scale eddies play an important role in ocean dynamics, but, unlike mesoscale eddies, they cannot be measured at present on a global scale. Therefore all present studies of small-scale eddies can only be case studies. The hope is that with the future instrument SWOT (Surface Water and Ocean Topography) (http://swot.jpl.nasa.gov/) small-scale eddies can be measured on global scale independently of cloud coverage and time of the day. This instrument is scheduled to be launched in 2020. It is a wide-swath altimeter using the SAR principle. The goal is to achieve an accuracy of geostrophic velocity measurements (via SLA measurements) of 0.03 m s^{-1} at a horizontal scale of 10 km at 45° latitude (Fu & Ferrari, 2008). Thus SWOT would allow, in conjunction with high resolution ocean models, the study of small-scale oceanic eddies on a global scale and thus improve fisheries and ecosystem management strongly linked to primary production.

Acknowledgments

This study was supported by BMBF-Ib and AIRD grants obtained to build the Trilateral German–French–African Environmental research initiatives in Sub-Sahara Africa entitled AWA “Ecosystem Approach to the management of fisheries and the marine environment in West African waters” (www.awa-project.org). Additional support was provided by BMBF grant FKZ 03F0611A. We thank J. Lilly for their discussion and help with the drifter analysis and Florian Schütte for data processing. Mercator model output was provided by Mercator Ocean via contract 2011/SG/CUTD/56. We would like to thank ESA for providing the ASAR images free of charge. We also thank NASA/OBPG (MODIS/Aqua) and EUMETSAT/SAF-OSI (AVHRR/METOP, SEVIRI/MSG) for providing the SST and ocean color data through their data access facilities and P. Le Borgne (Météo-France, Centre de Météorologie Spatiale, Lannion) for his advice in SST processing. The drifter was deployed as part of the ONR-funded COCES and COCES-II projects corresponding to grant numbers N000140811038 and N000141110480. Special thanks to Milena Menna for the processing of the drifter data.

References

Alpers, W., Espedal, H., & Apel, J. R. (2004). Oils and surfactants, chapter 11 in Synthetic Aperture Radar Marine User's Manual. In Ch. R. Jackson (Ed.), Washington, D.C., USA: National Oceanic and Atmospheric Administration, Center for Satellite Application and Research, NOAA/NESDIS0-16-073214-X.

Alpers, W., Ivanov, A. Yu., & Dagestad, K. F. (2011). Encounter of foehn wind with an atmospheric eddy over the Black Sea as observed by the synthetic aperture radar onboard Envisat. *Monthly Weather Review*, *139*, 3992–4000.

Atwood, E., Duffy-Anderson, J. T., Horne, J. K., & Ladd, C. (2010). Influence of mesoscale eddies on ichthyoplankton assemblages in the Gulf of Alaska. *Fisheries Oceanography*, *19*, 493–507.

Bassin, C. J., Washburn, L., Brzezinski, M., & McPhee-Shaw, E. (2005). Sub-mesoscale coastal eddies observed by high frequency radar: A new mechanism for delivering nutrients to kelp forests in the Southern California Bight. *Geophysical Research Letters*, *32*, L12604. http://dx.doi.org/10.1029/2005GL023017.

Capet, X., McWilliams, J. C., Molemaker, M. J., & Shchepetkin, A. F. (2008). Mesoscale to submesoscale transition in the California Current System: I. Flow structure, eddy flux, and observational tests. *Journal of Physical Oceanography*, *38*, 29–43.

Chaigneau, A., Eldin, G., & Dewitte, B. (2008). Eddy activity in the four major upwelling systems from satellite altimetry (1992–2007). *Progress in Oceanography*, *83*, 117–123.

Chelton, D. B., de Szoeke, R. A., Schlax, M. G., Naggar, K. E., & Siwertz, N. (1998). Geographical variability of the first-baroclinic Rossby radius of deformation. *Journal of Physical Oceanography*, *28*, 433–460.

Chelton, D. B., Gaube, P., Schlax, M. G., Early, J. J., & Samelson, R. M. (2011a). The influence of nonlinear mesoscale eddies on near-surface oceanic chlorophyll. *Science*, *334*, 328–332.

Chelton, D. B., Schlax, M. G., & Samelson, R. M. (2011b). Global observations of nonlinear mesoscale eddies. *Progress in Oceanography*, *91*, 167–216.

Clemente-Colon, P., & Yan, X. H. (1999). Observations of east coast upwelling conditions in synthetic aperture radar imagery. *IEEE Transactions on Geoscience and Remote Sensing*, *37*, 2239–2248.

Cresswell, G. R., & Legeckis, R. (1986). Eddies off southeastern Australia. *Deep Sea Research Part A. Oceanographic Research Papers*, *33*, 1527–1562.

Cushman-Roisin, B., Tang, B., & Chassignet, E. (1990). Westward motion of mesoscale eddies. *Journal of Physical Oceanography*, *20*, 758–768.

D'Asaro, E. A. (1988). Observations of small eddies in the Beaufort Sea. *Journal of Geophysical Research*, *93*, 6669–6684.

Davies, P. A., Dakin, J. M., & Falconer, R. A. (1995). Eddy formation behind a coastal headland. *Journal of Coastal Research*, *11*, 154–167.

Demarcq, H. (1998). Spatial and temporal dynamic of the upwelling off Senegal and Mauritania: Local change and trend. In M. -H. Durand, P. Cury, R. Mendelssohn, C. Roy, A. Bakun, & D. Pauly (Eds.), *Global versus local changes in upwelling systems* (pp. 149–166). Paris: Orstom ed.

Denniss, T., Middleton, J. H., & Manasseh, R. (1994). Recirculation in the lee of complicated headlands: A case study of Bass Point. *Journal of Geophysical Research*, *100*(C8), 16087–16101.

DiGiacomo, P. M., & Holt, B. (2001). Satellite observations of small coastal ocean eddies in the Southern California Bight. *Journal of Geophysical Research*, *106*(C10), 22521–22543.

Early, J. J., Samelson, R. M., & Chelton, D. B. (2011). The evolution and propagation of quasigeostrophic ocean eddies. *Journal of Physical Oceanography*, *41*, 1535–1555.

Eldevik, T., & Dysthe, K. B. (2002). Spiral eddies. *Journal of Physical Oceanography*, *32*, 851–869. http://dx.doi.org/10.1175/1520-0485.

Espedal, H., Johannessen, O. M., Johannessen, J. A., Dano, E., Lyzenga, D., & Knulst, J. C. (1998). COASTWATCH'95: A tandem ERS-1/2 SAR detection experiment of natural film on the ocean surface. *Journal of Geophysical Research*, *103*, 24969–24982.

Falkowski, P. G., Ziemann, D. Z., Kolbera, Z., & Bienfang, P. K. (1991). Role of eddy of pumping in enhancing primary production in the ocean. *Nature*, *352*, 55–58.

Fu, L. -L., & Ferrari, R. (2008). Observing oceanic submesoscale processes from space. *Eos*, *89*(48), 488–489.

Fu, L. -L., & Holt, B. (1983). Some examples of detection of oceanic mesoscale eddies by the Seasat synthetic aperture radar. *Journal of Geophysical Research*, *88*, 1844–1852.

Godø, O. R., Samuelsen, A., Macaulay, G. J., Patel, R., Hjøllo, S. S., et al. (2012). Mesoscale eddies are oases for higher trophic marine life. *PLos One*, *7*(1), e30161. http://dx.doi.org/10.1371/journal.pone.0030161.

Gower, J. F. R., Denman, K. L., & Holyer, R. L. (1980). Phytoplankton patchiness indicates the fluctuations spectrum of mesoscale oceanic structure. *Nature*, *288*, 157–159.

Greenwood, J. E., Feng, M., & Waite, A. M. (2007). A one-dimensional simulation of biological production in two contrasting mesoscale eddies in the south eastern Indian Ocean. *Deep Sea Research Part II: Topical Studies in Oceanography*, *54*, 1029–1044.

Gruber, N., et al. (2011). Eddy-induced reduction of biological production in eastern boundary upwelling systems. *Nature Geoscience*, *4*, 787–792.

Hansen, D., & Poulain, P. -M. (1996). Quality control and interpolations of WOCE-TOGA drifter data. *Journal of Atmospheric and Oceanic Technology*, *13*, 900–909.

Heywood, R. B., & Priddle, J. (1987). Retention of phytoplankton by an eddy. *Continental Shelf Research*, *71*, 937–955.

Huehnerfuss, H., Alpers, W., Dannhauer, H., Gade, M., Lange, Ph. A., Neumann, V., et al. (1996). Natural and man-made sea slicks in the North Sea, investigated by a helicopter-borne 5-frequency radar scatterometer. *International Journal of Remote Sensing*, *17*, 1567–1582.

Ivanov, A. Yu., & Ginzburg, A. I. (2002). Oceanic eddies in synthetic aperture radar images, in: Proceedings of the Indian Academy of Sciences. *Earth and Planetary Sciences*, *111*(3), 281–295.

Johannessen, J. A., Roed, L. P., & Wahl, T. (1993). Eddies detected in ERS-1 SAR images and simulated in reduced gravity model. *International Journal of Remote Sensing*, *14*, 2203–2213.
Johannessen, J. A., Shuchman, R. A., Digranes, G., Lyzenga, D., Wackerman, C., Johannessen, O. M., et al. (1996). Coastal ocean fronts and eddies imaged with ERS-1 synthetic aperture radar. *Journal of Geophysical Research*, *101*, 6651–6667.
Karimova, S. (2012). Spiral eddies in the Baltic, Black and Caspian seas as seen by satellite radar data. *Advances in Space Research*, *50*(8), 1107–1124.
Kasajima, K., et al. (2006). A submesoscale coherent eddy in the Greenland Sea in 2003. *Journal of Geophysical Research*, *111*, C07013. http://dx.doi.org/10.1029/2005JC003130.
Kaz'min, A. S., & Kuz'mina, N. P. (1990). Certain features of small-scale oceanic eddies derived from satellite imagery analysis. *Soviet Journal of Remote Sensing*, *6*, 13–18.
Keller, W. C., Wismann, V., & Alpers, W. (1989). Tower-based measurements of the ocean C-band radar backscattering cross section. *Journal of Geophysical Research*, *94*, 924–930.
Korotaev, G. K., & Fedotov, A. (1994). Dynamics of an isolated barotropic vortex on a beta-plane. *Journal of Fluid Mechanics*, *264*, 277–301.
Kozlov, I. E., Kudryavtsev, V. N., Johannessen, J. A., Chapron, B., Dailidiene, I., & Myasoedov, A. G. (2012). ASAR imaging for coastal upwelling in the Baltic Sea. *Advances in Space Research*, *50*(8), 1125–1137.
Ladd, C., Crawford, W. R., Harpold, C. E., Johnson, W. K., Kachel, N. B., et al. (2009). A synoptic survey of young mesoscale eddies in the Eastern Gulf of Alaska. *Deep Sea Research Part II: Topical Studies in Oceanography*, *56*, 2460–2473.
Lam, J. S. -L., & Dritschel, D. (2001). On the beta-drift of an initially circular vortex patch. *Journal of Fluid Mechanics*, *436*, 107–129.
Large, W. G., & Pond, P. (1981). Open ocean momentum flux measurements in moderate to strong winds. *Journal of Physical Oceanography*, *11*, 324–336.
Lathuilière, C., Levy, M., & Echevin, V. (2011). Impact of eddy-driven vertical fluxes on phytoplankton abundance in the euphotic layer. *Journal of Plankton Research*, *33*(5), 827–831.
Le Galloudec, O., Bourdalle-Badie, R., Drillet, Y., Derval, C., & Bricaud, C. (2008). Simulation of meso-scale eddies in the Mercator global ocean high resolution model. *Mercator Newsletter*, *3*.
Lellouche, J. -M., Le Galloudec, O., Drévillon, M., Régnier, C., Greiner, E., Garric, G., et al. (2012). Evaluation of real time and future global monitoring and forecasting systems at Mercator Océan. *Ocean Science Discussions*, *9*, 1123–1185.
Levy, M., Klein, P., & Treguier, A. M. (2001). Impact of sub-mesoscale physics on production and subduction of phytoplankton in an oligotrophic regime. *Journal of Marine Research*, *59*, 535–565.
Lévy, M., Klein, P., Tréguier, A. M., Iovino, D., Madec, G., Masson, S., et al. (2010). Modifications of gyre circulation by sub-mesoscale physics. *Ocean Modelling*, *34*, 1–15.
Lilly, J. M., & Gascard, J. (2006). Nonlinear processes in geophysics wavelet ridge diagnosis of time-varying elliptical signals with application to an oceanic eddy. *Nonlinear Processes in Geophysics*, *13*, 467–483.
Lilly, J. M., Scott, R. K., & Olhede, S. C. (2011). Extracting waves and vortices from Lagrangian trajectories. *Geophysical Research Letters*, *38*(L23605), 1–5.
Lin, I. -I., Lien, Ch. -C. h., Wu, Ch. -R., George, T. F., Wong, G. T. F., Huang, Ch. -W., et al. (2010). Enhanced primary production in the oligotrophic South China Sea by eddy injection. *Geophysical Research Letters*, *37*, L16602. http://dx.doi.org/10.1029/2010GL043872.
Lumpkin, R., & Pazos, M. (2007). Measuring surface currents with SVP drifters: The instrument, its data and some results. In A. Griffa (Ed.), *Lagrangian analysis and prediction of coastal and ocean dynamics* (pp. 39–67). : Cambridge University Press.
Mahadevan, A., Thomas, L. N., & Tandon, A. (2008). Technical comment: Eddy/wind interactions stimulate extraordinary mid-ocean plankton blooms. *Science*, *320*, 448b. http://dx.doi.org/10.1126/science.1152111.
Maltrud, M. E., & McClean, J. L. (2005). An eddy resolving global 1/10° ocean simulation. *Ocean Modelling*, *8*(1–2), 31–54.
Marullo, S., Salusti, E., & Viola, A. (1985). Observations of a small-scale baroclinic eddy in the Ligurian Sea. *Deep Sea Research*, *32*, 215–222.
McWilliams, J. C. (1985). Submesoscale, coherent vortices in the ocean. *Reviews of Geophysics*, *23*, 165–182.
Morrow, R., Fang, F., Fieux, M., & Molcard, R. (2003). Anatomy of three warm-core Leeuwin current eddies. *Deep Sea Research Part II: Topical Studies in Oceanography*, *50*, 2229–2243.
Munchow, A. (2000). Wind stress curl forcing of the coastal ocean near Point Conception, California. *Journal of Physical Oceanography*, *30*, 1265–1280.
Munk, W., Armi, L., Fischer, K., & Zachariasen, F. (2000). Spirals on the sea. *Proceedings of the Royal Society of London. Series A*, *456*, 1217–1280.
Murdoch, R. C. (1989). The effects of a headland eddy on surface macro-zooplankton assemblages north of Otago Peninsula, New Zealand. *Estuarine, Coastal and Shelf Science*, *29*, 361–383.
Olson, D. B. (1991). Rings in the ocean. *Annual Review of Earth and Planetary Sciences*, *19*, 283–311.
Pattiaratchi, C., James, A., & Collins, M. (1987). Island wakes and headland eddies: A comparison between remotely sensed data and laboratory experiments. *Journal of Geophysical Research*, *92*, 783–794.
Perissinotto, R., & Rae, C. M. D. (1990). Occurrence of anticyclonic eddies on the Prince-Edward Plateau (Southern Ocean): Effects on phytoplankton biomass and production. *Deep Sea Research*, *37*, 777–793.
Romano, J. C., & Marquet, R. (1991). Occurrence frequencies of sea surface slicks at long and short time-scales in relation to wind speed. *Estuarine, Coastal and Shelf Science*, *33*, 445–458.
Rubino, A., & Brandt, P. (2003). Warm-core eddies studied by laboratory experiments and numerical modeling. *Journal of Physical Oceanography*, *33*, 431–435.
Rubino, A., Brandt, P., & Hessner, K. (1998). Analytical solutions for circular eddies of the reduced-gravity, shallow-water equations. *Journal of Physical Oceanography*, *28*, 999–1002.
Scott, R., Bourassa, M., Chelton, D., Cipollini, P., Ferrari, R., Fu, L. L., et al. (2010). Satellite altimetry and key observations: What we've learned, and what's possible with new technologies. In J. Hall, D. E. Harrison, & D. Stammer (Eds.), *ESA Publication, proceedings of the OceanObs09: Sustained ocean observations and information for society. Conference*, *vol. 2*. (pp. WPP-306) (Venice, Italy, 21–25 September 2009).
Scully-Power, P. (1986). *Navy oceanographer shuttle observations, STS 41-G, mission report*. Naval Underwater Systems Center technical report (NUSC TD 7611, 71 pp.).
Siegel, A., Weiss, J. B., Toomre, J., McWilliams, J. C., Berloff, P. S., & Yavneh, I. (2001). Eddies and vortices in ocean basin dynamics. *Geophysical Research Letters*, *28*, 3183–3186.
Signell, R. P., & Geyer, W. R. (1991). Transient eddy formation around headlands. *Journal of Geophysical Research*, *96*, 2561–2575.
Sikora, T. D., Young, G. S., & Winstead, T. S. (2006). A novel approach to marine wind speed assessment using synthetic aperture radar. *Weather and Forecasting*, *21*, 109–115.
Soules, S. D. (1970). Sun glitter viewed from space. *Deep Sea Research*, *17*, 191–195.
Stevenson, R. E. (1998). Spiral eddies: The discovery that changed the face of the oceans. *21st Century Science and Technology*, *11*, 58–71.
Stoffelen, A., & Anderson, D. (1997). Scatterometer data interpretation: Estimation and validation of the transfer function CMOD4. *Journal of Geophysical Research*, *102*, 5767–5780.
Thomas, L. N., Tandon, A., & Mahadevan, A. (2008). Submesoscale processes and dynamics. *Geophysical Monograph Series*, *177*, 17–38.
Valenzuela, G. R. (1978). Theories for the interaction of electromagnetic and ocean waves—A review. *Boundary-Layer Meteorology*, *13*, 61–85.
Wang, S., & Tang, D. (2010). Remote sensing of day/night sea surface temperature difference related to phytoplankton bloom. *International Journal of Remote Sensing*, *31*, 4569–4578.
Williams, R. G. (2011). Ocean eddies and plankton blooms. *Nature Geoscience*, *4*, 739–740.
Wismann, V., Gade, M., Alpers, W., & Huehnerfuss, H. (1998). Radar signatures of marine mineral oil spills measured by an airborne multi-frequency multi-polarization microwave scatterometer. *International Journal of Remote Sensing*, *19*, 3607–3623.
Yamaguchi, S., & Kawamura, H. (2009). SAR-imaged spiral eddies in Mutsu Bay and their dynamic and kinematic models. *Journal of Physical Oceanography*, *65*(4), 525–539.
Yang, X., Li, X., Li, Z., & Pichel, W. (2011). The impact of ocean surface features on the high resolution wind. *Proceedings of the 2011 international geoscience and remote sensing symposium (IGARSS 2011)* (978-1-4577-1005-6/11/$26.00 ©2011 IEEE).
Zhang, H. -M., Bates, J. J., & Reynolds, R. W. (2006). Assessment of composite global sampling: Sea surface wind speed. *Geophysical Research Letters*, *33*, L17714. http://dx.doi.org/10.1029/2006GL027086.